Journal of
Materials Chemistry A

Materials for energy and sustainability

rsc.li/materials-a

ROYAL SOCIETY
OF **CHEMISTRY**
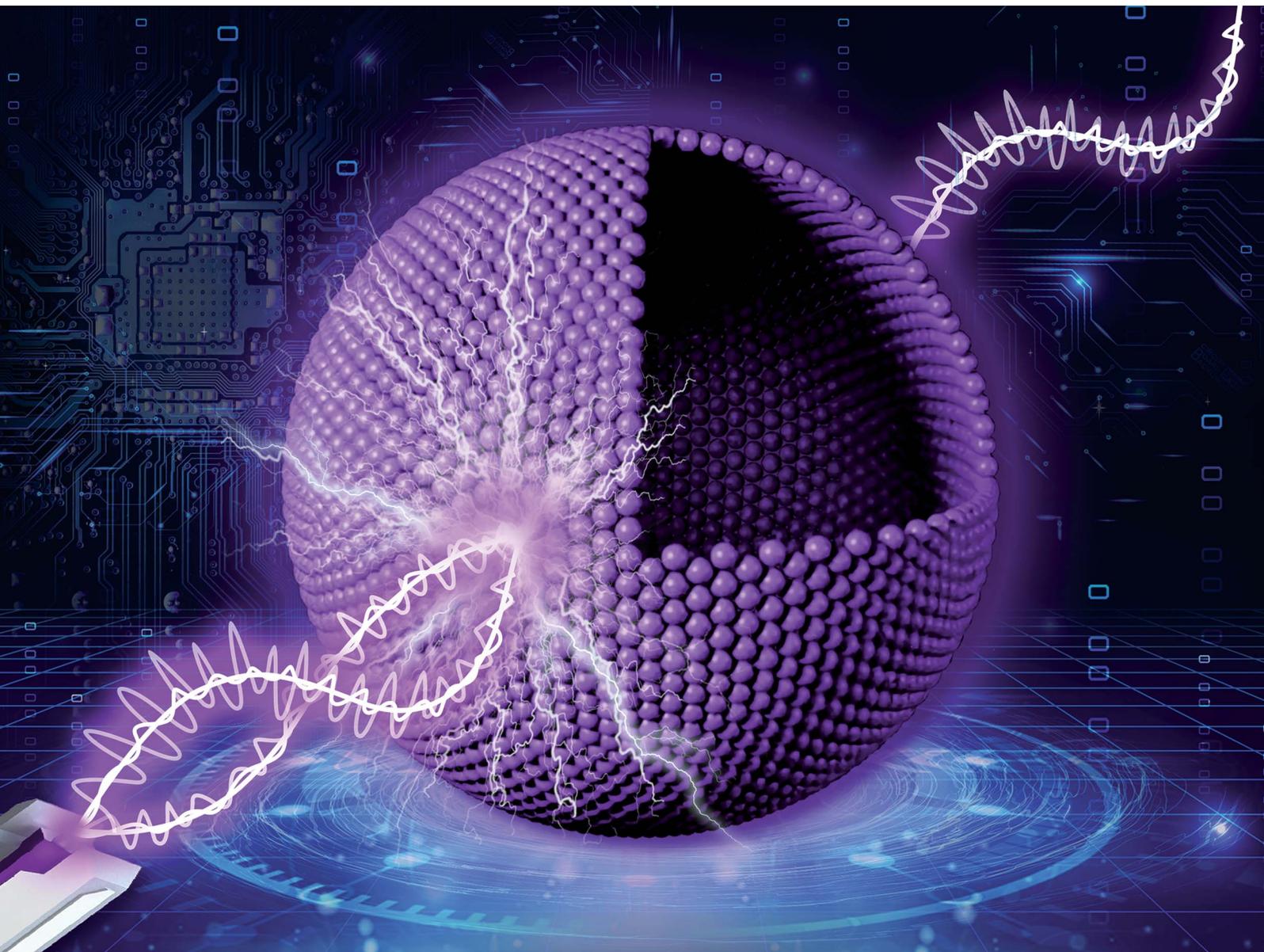
PAPER
Wenhuan Huang, Renchao Che, Huabin Zhang *et al.*
Hollow MoC/NC sphere for electromagnetic wave
attenuation: direct observation of interfacial polarization
on nanoscale hetero-interfaces

PAPER

Check for updates

Hollow MoC/NC sphere for electromagnetic wave attenuation: direct observation of interfacial polarization on nanoscale hetero-interfaces†

Wenhuan Huang, [ID] *[a] Wenming Gao,[ab] Shouwei Zuo,[ab] Luxi Zhang,[a] Ke Pei,[d] Panbo Liu, [ID] [c] Renchao Che [ID] *[d] and Huabin Zhang [ID] *[b]

Carbon-based composites with hetero-interfaces is a group of promising electromagnetic wave absorbing materials (EWAMs) for their excellent dielectric loss. For developing this kind of EWAMs, *in situ* construction of hetero-interfaces and revealing its attenuation mechanism are of great importance, but remain challenges. Herein, a MoC-incorporated N-doped carbon hollow sphere (H-MoC/NC) with uniformly distributed nanoscale MoC/NC hetero-interfaces was precisely synthesized for evaluating the interfacial polarization in electromagnetic wave attenuation. The Mo defects in MoC not only contributed to the impedance matching through the hollow shell, but also accelerated the charge transfers, displaying an enhanced interfacial charge polarization. More importantly, this polarized charge distribution on the MoC(−)/carbon(+) interface was observed for the first time directly through the hologram at a nanometer scale. The atomic-level understanding of interfacial polarization in the electromagnetic attenuation process will greatly promote the development of designing and synthesizing non-magnetic carbon-based EWAMs.

Introduction

For solving the spatial electromagnetic radiation, in recent decades, scientists have developed numerous groups of highly efficient electromagnetic wave absorbing materials (EWAMs), including carbon-based materials,[1–3] silicon carbides,[4,5] transition metal-based carbides,[6,7] oxides,[8,9] sulfides,[10,11] nitrides,[12,13] and ferromagnetic metal-based materials.[14–16] In the electromagnetic wave absorbing process, the combination of permittivity and permeability directly determines the electromagnetic wave storage and attenuation capacities of the materials.[17–21] It is an overall synergetic effect of intrinsic electrical and magnetic characteristics modulated by chemical-components, electron conductivity, electromagnetic balance, and micro-nano structure.[22–27] Therefore, for the rational design and synthesis of

EMAMs with the target properties, investigating the mechanism of attenuation contribution of each part is necessary.[11,28–31]

The permeability of the materials generally can be evaluated by magnetizability and saturation magnetization from magnetic hysteresis loops.[14,32,33] Moreover, off-axis electron holography and micromagnetic simulation can also be utilized to confirm the magnetic coupling between metal nanoparticles.[14,33] As another part of attenuation contribution, permittivity attenuation consists of several parts, including conduction loss, dipole polarization loss, and interfacial polarization loss.[6,34] Among them, conduction loss is mainly due to the conductivity of the materials, which can be tested through a four-probe resistance meter.[17,35] The dipole polarization is attributed to the chemical bond or atom–atom interaction in hybrids, which can be investigated by X-ray photoelectron- and Fourier transform infrared spectroscopy.[34,36] For studying the attenuation mechanism of interfacial polarization, numerous physical and chemical strategies have been employed for constructing hetero interfaces in composites.[2,37–40] Some interfacial interactions have already been investigated, such as the coupling between Sn-graphitized/amorphous carbon was evaluated by EXAFS,[17] and the interaction in the 2H-MoS₂/1T-MoS₂ interface was evaluated by the EPR results.[10] Some excellent synthesis strategies for constructing hetero-interfaces have been applied for enhancing the conversion of electrochemical energy and electromagnetic wave energy.[41–46] Recently, the polarized charge distribution of ZnO/Ni interfaces was directly observed by a hologram, but the visible range of polarization interfaces was

[a]Key Laboratory of Chemical Additives for China National Light Industry, College of Chemistry and Chemical Engineering, Shaanxi University of Science and Technology, Xi'an 710021, China. E-mail: huangwenhuan@sust.edu.cn

[b]KAUST Catalysis Center, King Abdullah University of Science and Technology, Thuwal, 23955-6900, Kingdom of Saudi Arabia. E-mail: huabin.zhang@kaust.edu.sa

[c]School of Chemistry and Chemical Engineering, Northwestern Polytechnical University, Xi'an 710129, China

[d]Laboratory of Advanced Materials, Shanghai Key Lab of Molecular Catalysis and Innovative Materials, Fudan University, Shanghai 200438, P. R. China. E-mail: rcche@fudan.edu.cn

† Electronic supplementary information (ESI) available. See DOI: 10.1039/d1ta09357f

about 100 nm, which lay between hetero-particles.[22] Under such circumstances, the internal polarization mechanism at an atomic level on a hetero-interface cannot be directly observed and investigated.[9,17,36,47]

Herein, nanoscale hetero-interfaces in a MoC-incorporated N-doped carbon hollow sphere (H-MoC/NC) were elaborately designed and constructed for investigating the internal mechanism of interfacial polarization and clarifying its contribution in permittivity attenuation.[10] As a unique feature, a ZnMo-bimetallic hybrid zeolitic imidazolate framework (HZIF-ZnMo), which is a representative of a new class of metal organic frameworks (MOF) with orderly arranged MoO_4 in the crystalline structure of the zeolite imidazolate framework (ZIF), was employed as a precursor to construct MoC/NC hetero-interfaces.[48,49] Moreover, by introducing a chemical etching step, the hollow sphere (H-MoC/NC) was assembled to obtain nanoscale MoC/NC interfaces and survey the interfacial polarization mechanism at the atomic level.[15] As a result, the Mo defects on the hetero-interfaces were observed, which resulted in the interfacial polarization by charge transfer and charge accumulation. More importantly, this interfacial charge polarization at the MoC/NC interface around ~1 nm was directly observed through the hologram. To the best our knowledge, it is the first time to investigate and understand the interfacial polarization from the atomic level.

Experimental

Synthetic procedures

Synthesis of the HZIF-ZnMo precursor. According to a typical procedure,[48] the mixture of $Zn(CH_3COO)_2$ $2H_2O$ (5.28 g, 24 mmol), 2-mim (2.88 g, 36 mmol), H_2MoO_4 (0.99 g, 6 mmol) and 120 mL DMF was kept stirring at 160 °C for 6 h in a 250 mL round bottom flask. After natural cooling the mixture, a white HZIF-ZnMo powder product was obtained with 35% yield. The powder was filtered and washed by ethanol for three times, and then dried at room temperature. In contrast, ZIF-Zn was synthesized (in ESI†).

Synthesis of H-HZIF-ZnMo. HZIF-ZnMo (0.3 g) was dispersed into the solution of 1.5 g tannic acid and 300 mL water, and then kept stirring for 10 min. The product of H-HZIF-ZnMo was centrifuged and washed by water and ethanol separately for three times. After drying in vacuum oven at 60 °C for 3 h, the 250 mg of earthy yellow H-HZIF-ZnMo powder was obtained. Similarly, H-ZIF-Zn was also synthesized (in ESI†).

Synthesis of H-MoC/NC. 500 mg of the as synthesized H-HZIF-ZnMo was placed in corundum boats and heated to 900 °C at a rising rate of 8 °C min⁻¹ in a tube furnace under nitrogen flow. After it was kept at 900 °C for 2 h. The black powder of H-MoC/NC was obtained. The calcination results of H-NC, MoC/NC, NC are listed in SI.

Characterization and data analysis

Characterizations. A D8 DAVANCI X-ray powder diffractometer was used to record the powder X-ray diffraction (PXRD) patterns. The specific surface area was measured by nitrogen adsorption and desorption at 77 K by an ASAP 2020 sorption system. Scanning electron microscopy (SEM) images were collected on a Hitachi S4800 apparatus. The transmission electron microscopy (TEM) was performed on a JEM-2010HR apparatus, and X-ray energy-dispersive spectroscopy (EDS) was performed on a JEM-2010HR-Vantage type energy spectrometer. X-ray photoelectron spectroscopy (XPS) was implemented on a Thermo ESCA Lab250XI. Raman spectroscopy was obtained by a Renishaw inVia Raman Microscope. The electromagnetic parameters were analysed by a HP8753D vector network analyser. The measured samples were dispersed in paraffin homogeneously with a sample-to-paraffin weight ratio of 3 : 17 (loading amount of 15 wt%), and then, the mixture was pressed into a toroidal shape with an inner diameter of 2.0 mm and an outer diameter of 7.0 mm.

Data analysis. The Cole–Cole semicircle model, Debye theory and Debye relaxation correction formula, attenuation coefficient, transmission line theory, quarter-wavelength matching model were employed for analysing the electromagnetic wave absorbing performance. The data analysis details are listed in ESI.†

Results and discussion

Synthesis and structural characterization

The synthesis procedure of the hollow MoC-incorporated N-doped carbon (H-MoC/NC) sphere is illustrated in Fig. 1. For evaluating the attenuation mechanism of the MoC/NC hetero-interface in the hollow structure, solid MoC-incorporated N-doped carbon (MoC/NC), hollow N-doped carbon (H-NC) and solid N-doped carbon (NC) were elaborately synthesized and characterized as contrast samples. The HZIF-ZnMo was crystallized from MoO_4, Zn and imidazole (Fig. 1a₁), while ZIF-Zn was assembled from Zn and imidazole (Fig. 1b₁), which, as precursors (Fig. S1†), were calcinated at 900 °C under nitrogen flow, and transformed into solid MoC/NC and NC polyhedrons (Fig. 1a₂ and b₂). As shown in Fig. 2a and b, solid MoC/NC and NC kept the original shapes of HZIF-ZnMo and ZIF-Zn, showing a chamfered cube and a rhombohedral dodecahedron with diameters of 2 μm and 500 nm, respectively. The uniformly distributed elements were evaluated by EDS mapping in Fig. S3, S4, S7 and S8.†

For constructing the hollow structure, an acid etching process was employed, which successfully generated the HZIF-ZnMo hollow sphere (H-HZIF-ZnMo) and the ZIF-Zn hollow rhombohedral dodecahedron (H-ZIF-Zn) (Fig. 1a₃ and b₃).[50,51] SEM and TEM results in Fig. 2b₃ indicate that H-ZIF-Zn perfectly inherited the morphology of ZIF-Zn with an ultra-thin shell after the etching process. As illustrated in Fig. 1d, the fast formed ZnO_x shell protected the surface of ZIF-Zn; hence, a hollow polyhedron was formed during a fast ion-diffusion process. On the contrary, owing to the higher chemical stability than those of ZIF-Zn, HZIF-ZnMo was slowly decomposed and accompanied by the formation of a ZnO_x/MoO_x oxide shell, displaying a slow ion-diffusion speed (Fig. 1c).[48,52,53] This slow surface solvation process generated a hollow sphere morphology of H-HZIF-ZnMo (Fig. 2a₃). Then, after the same calcination
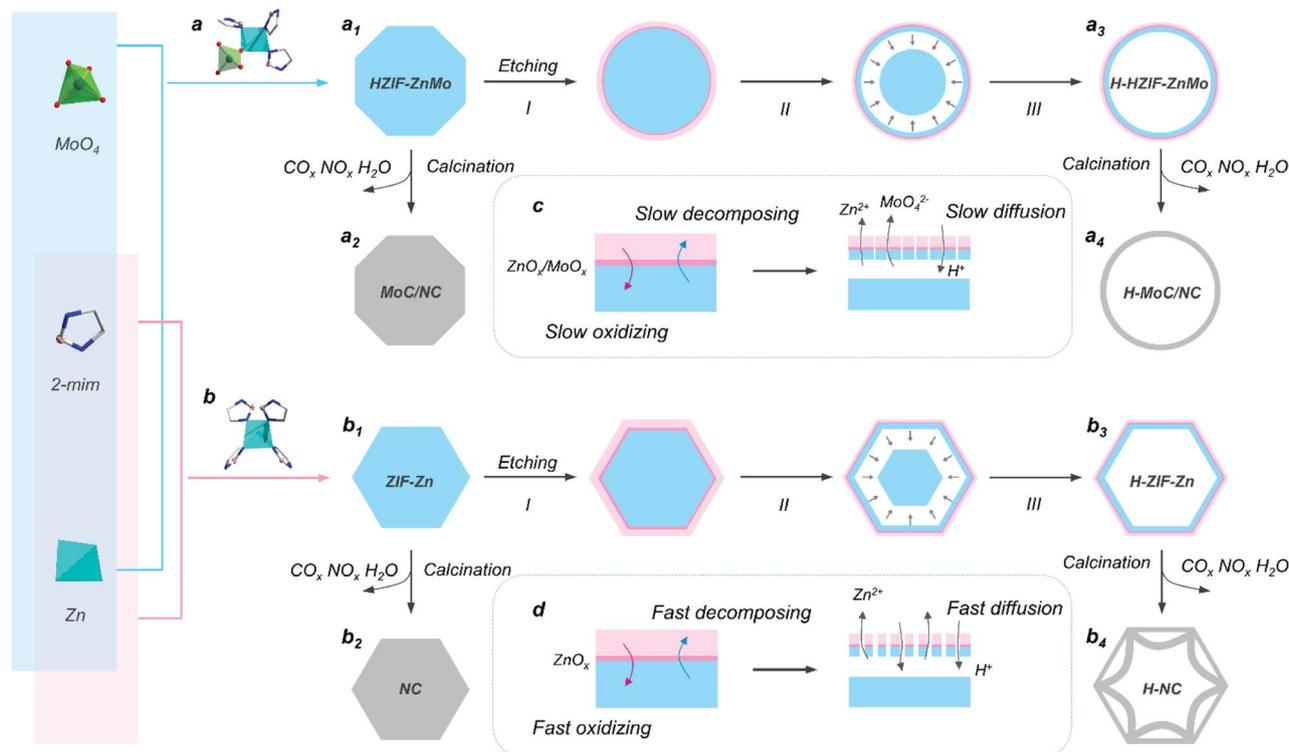
This journal is © The Royal Society of Chemistry 2022

J. Mater. Chem. A, 2022, **10**, 1290–1298 | **1291**

Fig. 1 (a) and (b) The crystalline structure of HZIF–ZnMo and ZIF-Zn. (a$_1$–a$_4$) The schematic morphologies for HZIF–ZnMo, MoC/NC, H–HZIF–ZnMo and H-MoC/NC. (b$_1$–b$_4$) The schematic morphologies for ZIF-Zn, NC, H-ZIF-Zn and H-NC; (c and d) the chemical etching process schemes for HZIF–ZnMo and ZIF-Zn.

condition at 900 °C, H-HZIF-ZnMo and H-ZIF-Zn were *in situ* transformed into hollow structural H-MoC/NC and H-NC particles (Fig. 2a$_4$ and b$_4$). The good thermal stability of HZIF-ZnMo and the MoC component resulted in the remained hollow sphere morphology of H-MoC/NC (Fig. 2a$_4$). However, during the fast decomposition of H-ZIF-Zn and departure of the gases, the shrunken hollow rhombohedral dodecahedron morphology of H-NC (Fig. 2b$_4$) was obtained. These results were also confirmed by IV-type N$_2$ sorption isotherm curves and micropores in pore diameter results (Fig. 2d and e). The pore size of the hollow structural H-MoC/NC and H-NC samples were obviously larger than that of solid MoC/NC and NC samples. The higher BET surface area of H-MoC/NC (582.425 m^2 g^{-1}) and that of un-calcinated H-HZIF-ZnMo (217.129 m^2 g^{-1}) meant the increase in the pore volume and the maintained hollow sphere morphology after the calcination. Moreover, the smaller surface area of H-NC (960.190 m^2 g^{-1}) than that of un-calcinated H-ZIF-Zn (1003.293 m^2 g^{-1}) proved the decrease in the pore volume and the shrinkage of H-NC.

HZIF-ZnMo was selected as a precursor for *in situ* synthesizing MoC-incorporated carbon owing to its high-crystalline structure of ordered arranged Zn, Mo and organic ligands. The crystalline phase of MoC and graphite carbon in both H-MoC/NC and MoC/NC were confirmed by the PXRD pattern (Fig. S11†). The wide peak at 21.3 corresponds to the (002) plane of graphite carbon, while the peaks at 36.6, 42.4, 61.8, and 74.3 are correspond to the (111), (200), (220), and (311) planes of α-

MoC (JCPDS-01-089-2868). As is known, the crystalline phase conversion for molybdenum carbide is observed during the high-temperature calcination process at 900 °C. Herein, a programmed heating process was employed for obtaining the pure phase of α-MoC, in which Mo and C atoms crystalized in the cubic $Fm\bar{3}m$ space group with the fcc stacking mode (Fig. 2f). The I_D/I_G ratio of D band (1350 cm^{-1}) and G band (1590 cm^{-1}) peaks were calculated from the Raman results (Fig. S12†) for characterizing the amount of the disordered/defected carbon and sp^2 carbon. The calculated higher I_D/I_G values for H-MoC/NC and H-NC (1.07 and 1.12) than those of solid MoC/NC and NC (0.94 and 1.03) indicates that the structural disorder and defects of the carbon matrix were more apparent in hollow structural samples.

On the other hand, chemical etching and calcination was used for constructing atomic defects and nanoscale hetero-interfaces. As the HRTEM results shown in Fig. 2c$_1$, abundant nanoscale H-MoC/NC hetero-interfaces were observed. MoC nanoparticles with the diameter of 2.5 nm were embedded with the carbon shells (Fig. 2c$_2$ and c$_3$). The atom arrangement highly matched with the (111) lattice plane of the MoC crystalline structure (Fig. 2c$_4$). In the MoC particle, numerous Mo defects in the lattice were observed, which benefited the electron hopping and charge transfer. Then, this was confirmed by the XPS results (Fig. 2g and h). The Mo 3d XPS spectra split into 3d$_{5/2}$ and 3d$_{3/2}$ peaks, which were further fitted into four oxidation states peaks of Mo^{2+}, Mo^{3+}, Mo^{4+} and Mo^{6+} (Fig. 2g).

1292 | *J. Mater. Chem. A*, 2022, **10**, 1290–1298

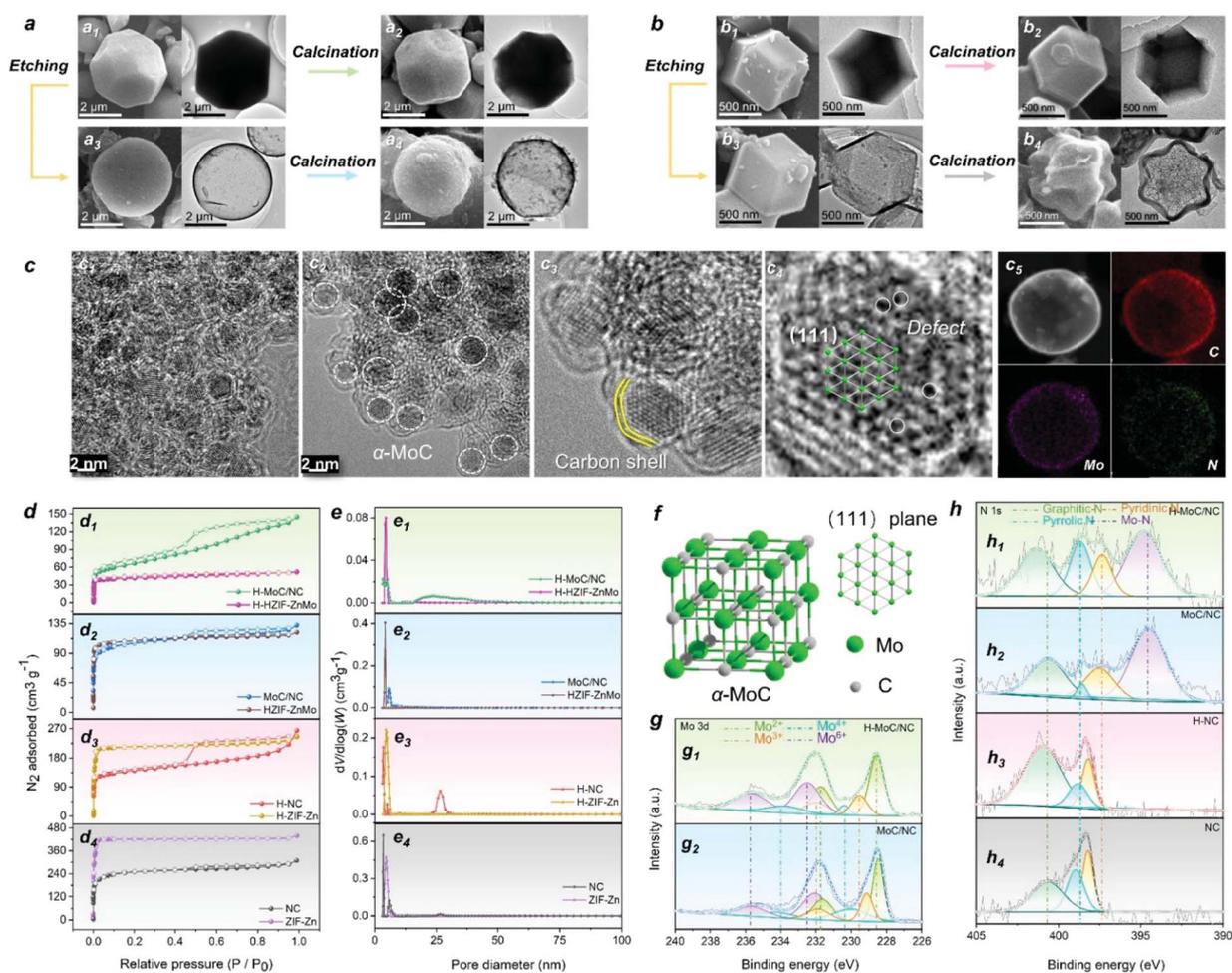This journal is © The Royal Society of Chemistry 2022

Fig. 2 (a) SEM and TEM images of HZIF-ZnMo (a_1), MoC/NC (a_2), H-HZIF-ZnMo (a_3) and H-MoC/NC (a_4). (b) SEM and TEM images of ZIF-Zn (b_1), NC (b_2), H-ZIF-Zn (b_3) and H-NC (b_4). (c) Hetero-interfaces in HR-TEM (c_1), the MoC nanoparticles (c_2), MoC@C structure (c_3), lattice and defects (c_4) and EDS mapping (c_5) images of H-MoC/NC. (d) N_2-sorption isotherms curves. (e) Pore diameter distribution curves. (f) Crystalline structure of α-MoC. (g) Mo 3d XPS spectra for H-MoC/NC and MoC/NC. (h) N 1s XPS spectra for H-MoC/NC, MoC/NC, H-NC and NC.

Owing to the existence of and Mo–C bonds in α-MoC, the Mo^{2+} peaks were observed. The Mo defects in the crystalline brought the valence state increase of the adjacent Mo atom sites, such as the emerging of Mo^{3+}, while the existence of Mo^{4+} and Mo^{6+} was attributed to the surface oxidation of MoO_x (MoO_2 and MoO_3). Compared with MoC/NC, the higher amount of high-valent Mo atoms and positive shifts of all Mo peaks for H-MoC/NC were attributed to the Mo defects, valence changes on the Mo–N/Mo–O bonds at the hetero-interfaces. The N 1s spectra for H-MoC/NC and MoC/NC (Fig. 2h) exhibited pyridinic N, pyrrolic N, graphitic and Mo–N peaks. The high amount of pyrrolic N, positive shift of graphitic N and Mo–N, and negative shift of pyridinic N in H-MoC/NC indicated the defects and disordered atoms. The doped N atoms in the carbon matrix provided the dipole polarization in the graphite carbon. The C 1s XPS spectra (Fig. S13†) displayed multiple C–O pieces in the hollow structural H-MoC/NC and H-NC. Compared with the MoC/NC, the higher C–N/C–C peak ratio and positive shift of C–N in H–MoC/NC also confirmed the disordered atoms in the carbon matrix.

Electromagnetic wave absorbing performance

The electromagnetic wave absorbing performance was evaluated by electromagnetic parameters of the samples in a paraffin wax ring with a loading amount of 15 wt%. For a nonmagnetic material system, the real part and imaginary part of permittivity (ε' and ε'') in the formula of relative complex permittivity ($\varepsilon_r = \varepsilon' - j\varepsilon''$) represent the storage and the dissipation capacities of the electro-magnetic wave, respectively, while the tan δ_ε (tan $\delta_\varepsilon = \varepsilon''/\varepsilon'$) acts the index for the dielectric loss. The dielectric loss combines both effects of conduction loss and polarization loss. The general trends of ε', ε'' and tan δ_ε in Fig. S14† exhibited the higher permittivity parameters for hollow structural H-MoC/NC and H-NC than those for solid MoC/NC and NC, which was attributed to the enhanced interfacial polarization loss from the hollow structure. As we know, the polarization loss includes interfacial polarization and dipole polarization. For solid MoC/NC and NC, the higher permittivity parameters for MoC/NC than NC were mainly due to the dipole polarization loss. Conductive loss of the material can be expressed in the free

This journal is © The Royal Society of Chemistry 2022

J. Mater. Chem. A, 2022, **10**, 1290–1298 | **1293**

electron formula, $\varepsilon'' \approx \sigma/2\pi f\varepsilon_0$. The higher ε'' of H-NC than that of H-MoC/NC indicates the primary conductive loss in H-NC. In general, the dielectric loss of these samples are the results of synergistic effects between the conduction and polarization loss.

The Cole–Cole semicircle model was used to explain the polarization relaxation process, which is expressed in eqn (S1).† In the ε'–ε'' curves, every semicircle stands for a Debye relaxation process. The high number of the semicircles for H-MoC/NC indicated its high dipole depolarization loss and the interfacial polarization (Fig. S15†). In addition, the long line tail in the ε'–ε'' curve of NC (Fig. 3a) also indicates its brilliant conduction loss contribution.

In order to further quantitatively evaluate the contribution of the polarization loss, the interfacial polarization was first analysed through the Debye relaxation correction formula (eqn (S2) and (S3)†). In the formula, A is defined as the interface factor that fitted from ε' values, standing for the interface polarization (Fig. S16†). The A values of samples have been calculated in Fig. 3b. The higher A values of 0.26 and 0.66 for H-MoC/NC and H-NC were observed, confirming the dominant interfacial polarization in hollow porous materials. Moreover, the higher A value of MoC/NC (0.073) than that of NC (0.005) is observed, which is attributed to the chemical hetero-interface polarization in MoC/NC.

Furthermore, the quantitative evaluation of the polarization contribution from ε'' values was also conducted by the Debye theory through the eqn (S4)–(S6).† First, the conductive contribution part (ε_c'') of the samples (Fig. 3c) was calculated by the four-electrode resistance test results (Fig. 3f) through eqn (S4).†

The conductivity sequence of NC > H-NC > H-MoC/NC > MoC/NC indicates the biggest contribution on conduction loss ε_c'' for NC from 5.54 to 0.62. Then, the polarization loss (ε_p'') of the samples was calculated through eqn (S5) and (S6),† which confirmed the dominant polarization effect (ε_p'') in H-NC and H-MoC/NC from 10.36 to 7.93 and 2.83 to 3.49, respectively (Fig. 3d). These results indicate the dominated hetero-interfacial polarization in H-MoC/NC. As a result, the integrated permittivity of the materials reflected in the attenuation coefficient (α), which could be calculated through eqn (S7).† The higher α value of the material indicated the stronger compositive electromagnetic wave attenuation ability, combining the permeability and permittivity. In accordance with the dielectric loss (Fig. 3h), the α value (Fig. 3g) sequence of H-NC > H-MoC/NC > MoC/NC > NC was observed, which meant that H-NC possessed the strongest EW attenuation ability.

Then, the electromagnetic wave absorbing performance of the materials was evaluated by reflection loss (RL) and $|Z_{in}/Z_0|$, which were calculated from electromagnetic parameters through eqn (S8) and (9).† Although H-NC possesses the strongest integrated dielectric loss (Fig. 3h), the best EW absorption capacity (RL$_{min}$ of 41.2 dB at 13.44 GHz) and widest effective absorption band (f_e, RL <−10 dB) of 5.2 GHz (from 11.76 GHz −16.96 GHz) of H-MoC/NC were observed in Fig. 4h and i. The H-NC displayed a RL$_{min}$ of −13.34 dB at 10.72 with the f_e band of 2.0 GHz (Fig. 4b, j), while the MoC/NC exhibited a RL$_{min}$ of −19.17 dB at 14.24 with the f_e band of 1.3 GHz (Fig. 4c, k). It was concluded that excessive permittivity stood in
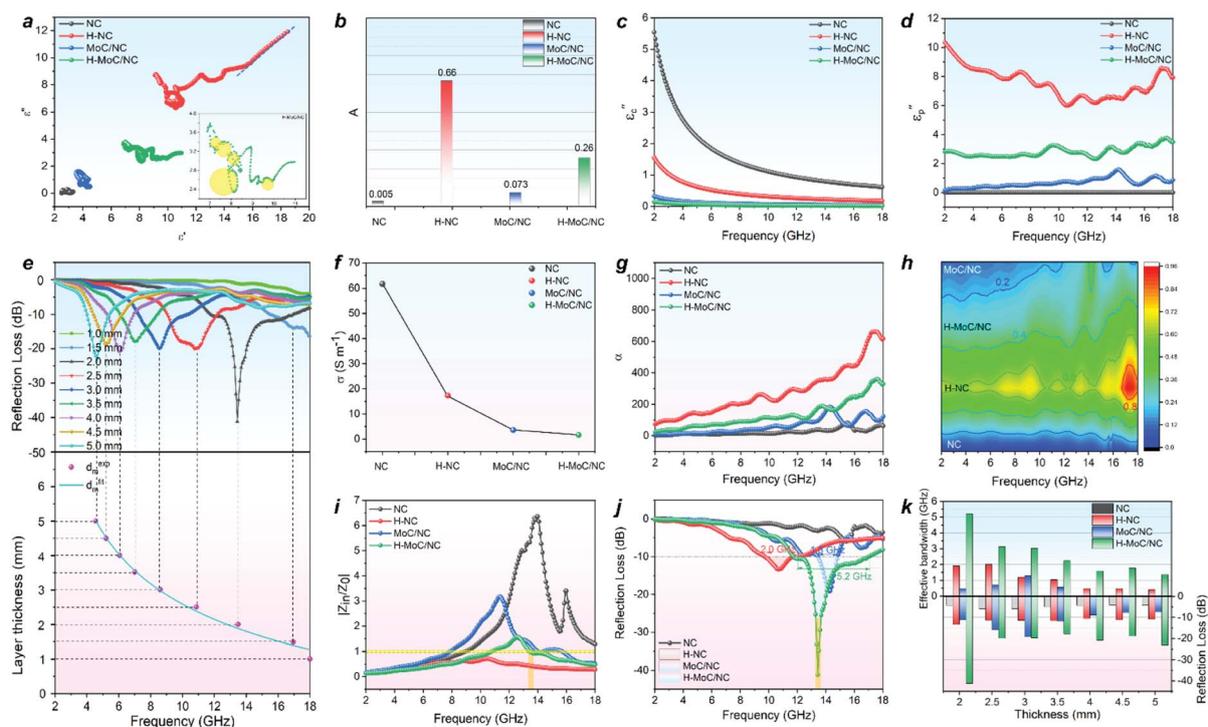

Fig. 3 The attenuation and impedance matching analysis. (a) Cole–Cole semicircle of H-MoC/NC (insert) in ε'–ε'' curves. (b) Calculated A values. (c) Calculated ε_c'' values. (d) Calculated ε_p'' values. (e) Experimental and theoretical fitted d_m values. (f) Conductivity. (g) Attenuation coefficient. (h) Dielectric loss. (i) Impedance matching plots. (j) The effective absorbing band (<−10 dB) in RL plots. (k) Effective bandwidth and minimum RL values.
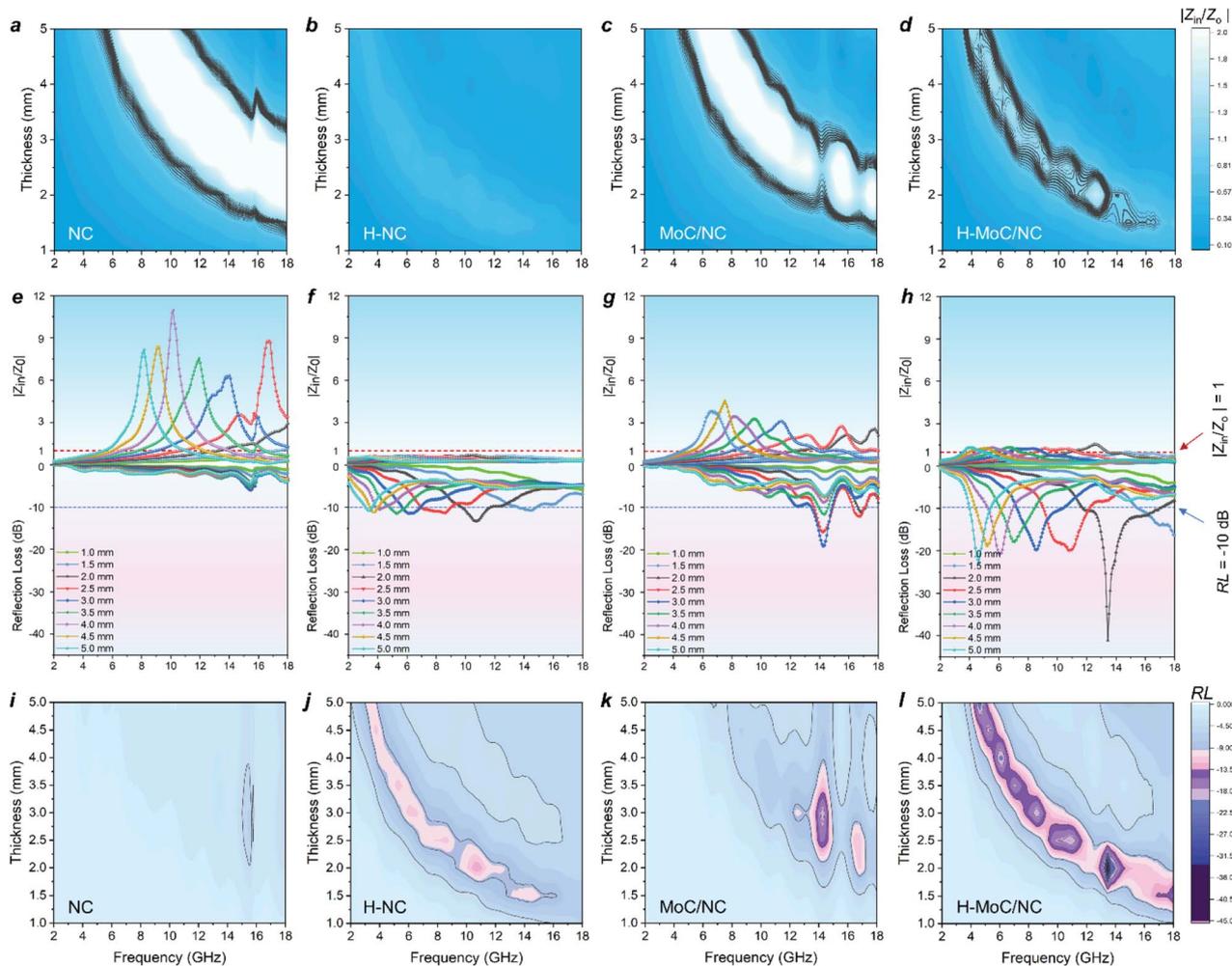
1294 | J. Mater. Chem. A, 2022, 10, 1290–1298

This journal is © The Royal Society of Chemistry 2022

Fig. 4 (a–d) 2D contour map of $|Z_{in}/Z_0|$ for NC, H-NC, MoC/NC and H-MoC/NC. (e–h) The $|Z_{in}/Z_0|$ and RL plots of NC, H-NC, MoC/NC and H-MoC/NC. (i–l) 2D contour map of RL for NC, H-NC, MoC/NC and H-MoC/NC.

the way of achieving high EM adsorption, and impedance matching of the materials played another crucial role.

The impedance matching of the materials could be evaluated by the normalized characteristic impedance ($Z = |Z_{in}/Z_0|$) based on eqn (S9).† The 2D contour map of Z values for all four materials are exhibited in Fig. 4a–d, in which the dark line ($Z = 0.8$–1.2) area indicates the good matching of the impedance. The excellent impedance matching of H–MoC/NC induced its high EW absorbing performance at the range of 4–18 GHz (Fig. 4d). The big white area in the 2D Z maps of MoC/NC and NC meant severe mismatches of impedance in the solid structures (Fig. 4a and c). Hollow structural H-NC greatly decreased the Z value, but not matched with the impedance (Fig. 4b). The synergetic effect from both the hollow space and hetero-interfaces of H-MoC/NC results in the best impedance matching and EW absorption (Fig. 3i–k). The high matching of theoretical and experimental d_m of H-MoC/NC (Fig. 3e) was verified through the quarter-wavelength formula (eqn S10).† As compared in Table S1 and Fig. S9,† H-MoC/NC displayed remarkable SR_L values of −275 at the thickness of 2 nm, making it one of the best Mo-based EWAM reported to date.

Based on the above studies, we can conclude that the polarization on MoC/NC hetero-interfaces in the hollow shell enhanced both the dielectric loss and impedance matching. In studies, scientists have successfully calculated the contribution of interfacial polarization in permittivity attenuation and proved its mechanism by spectroscopy characterizations; however, it has not been explained from an atomic level. In this study, the HR-TEM (Fig. 5e) and a hologram (Fig. 5a) were employed for investigating the mechanism of the interfacial polarization in H-MoC/NC. The tube area on the TEM image in Fig. 5a was the place that the beam lighted, which was the effective observing area. In the electric field distribution diagram (Fig. 5c), colour represents direction and brightness represents intensity, and the colour disk is shown in Fig. S20.† In the charge density map (Fig. 5d), red represents positive charge, blue represents negative charge, and the lightness colour represents relative density. The homogeneous distribution of the MoC is shown in Fig. 5e, and the high density of nanoscale MoC/NC interfacial polarization (2–3 nm) in the charge density map, as shown in Fig. 5d, which highly agreed with the distribution of MoC nanoparticles in the carbon
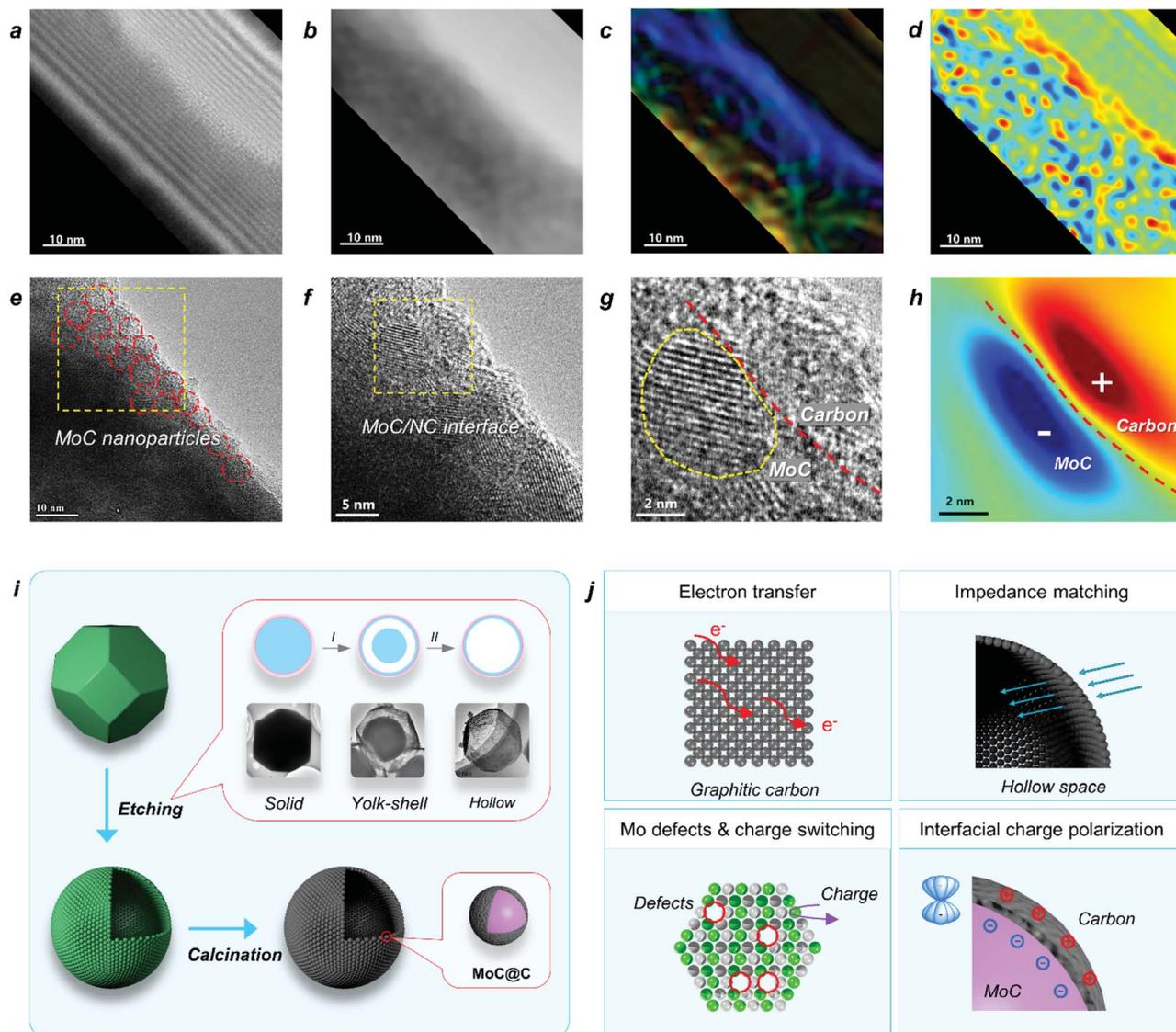
Fig. 5 (a) Hologram. (b) Reconstructed phase image. (c) Electric-filed map. (d) Charge density map. (e) HR-TEM images. (f and g) MoC/NC hetero-interface. (h) Charge distribution on the MoC(−)/carbon(+) interface. (i) Two-step synthetic route and chemical etching mechanism (insert). (j) Illustration schemes of four electromagnetic wave attenuation mechanism.

matrix. The hetero-interface between the MoC particle and carbon matric is clearly shown in Fig. 5g, while the corresponding charge density map (Fig. 5h) indicated the charge distribution along the hetero-interface. The Mo defects in MoC accelerated the charge transfer, resulting in the accumulation of the negative charge on the surface of MoC particles. Moreover, the positive shifts of the carbon atoms induced the positive charge on the surface of carbon matrix, generating the charge polarization between the MoC(−)/carbon(+) interfaces (Fig. 5h). It is the first time to observe and explain the interfacial polarization at a nano-meter scale.

Synthetic and electromagnetic wave absorbing mechanism

The mechanism of the two-step synthetic route for constructing a hollow MoC/N-doped carbon sphere with hetero-interfaces is displayed in Fig. 5i, including an acid etching and a high-temperature calcination process. First, through a diffusion/dissolution process HZIF-ZnMo polyhedron was in situ transformed into a HZIF-ZnMo hollow sphere. During the etching process, the yolk-shell intermediate HZIF-ZnMo was observed through the TEM images. Second, in the high-temperature calcination process, owing to the superior thermal stability and orderly arranged MoO_4 units in the crystalline structure of HZIF-ZnMo, a well-maintained MoC/NC hollow sphere was obtained. In the hollow shell, abundant MoC nanoparticles were embedded into the N-doped carbon matrix, affording nanometer level of hetero-interfaces.

The EW attenuation mechanism of H-MoC/NC is illustrated in Fig. 5j, which mainly included four aspects: (i) the fast electron transfer on graphite carbon contributed to the conductive

loss, resulting in the enhanced dielectric loss; (ii) the hollow space synergetic worked with dielectric loss, making H-MoC/NC to obtain the best impedance matching; (iii) the Mo defects in the MoC induced the charge switching of adjacent Mo atoms, enhancing the dipole polarization; (iv) Mo defects induced the accumulation of the negative charge on the surface of MoC, which strengthened the polarization on the MoC(−)/carbon(+) interface.

Conclusions

In summary, we subtly constructed a hollow MoC-incorporated N-doped carbon sphere (H-MoC/NC) with a nanoscale MoC(−)/NC(+) interface, as an EWAM, displaying a synergistic effect of conductive loss, dipole polarization loss, interfacial polarization and impedance matching. Through the accurate structural characterization and theoretical calculation, the dominate contribution of interfacial polarization on hetero-interfaces among MoC nanoparticles and N-doped carbon in the hollow shell was clarified. The Mo defects in the MoC lattice were observed, which directly enhanced the MoC(−)/carbon(+) interfacial polarization through charge switching and charge accumulation. To the best of our knowledge, it is the first time to observe and understand the interfacial polarization at the atomic level. Our findings open a new era, guiding the design and synthesis of highly efficient non-magnetic carbon-based EWAMs.

Author contributions

W. H. H. conceived the idea. W. M. G. and L. X. Z. carried out the materials synthesis. W. M. G., S. W. Z. and H. B. Z. conducted the materials characterizations and data analysis. W. H. H. performed the EW absorbing performance and calculations. K. P. and R. C. C. conducted the characterization and analysis for the holography images and charge density maps. W. H. H. wrote the manuscript. All authors read and commented on the manuscript.

Conflicts of interest

There are no conflicts to declare.

Acknowledgements

Notes and references

1 D.-X. Yan, H. Pang, B. Li, R. Vajtai, L. Xu, P.-G. Ren, J.-H. Wang and Z.-M. Li, *Adv. Funct. Mater.*, 2015, **25**, 559–566.

2 B. Quan, W. Shi, S. J. H. Ong, X. Lu, P. L. Wang, G. Ji, Y. Guo, L. Zheng and Z. J. Xu, *Adv. Funct. Mater.*, 2019, **29**, 1901236.

3 Y. Wan, X. Wang, X. Li, S. Liao, Z. Lin, Y. Hu, T. Zhao, X. Zeng, C. Li, S. Yu, P. Zhu, R. Sun and C. Wong, *ACS Nano*, 2020, **14**, 14134–14145.

4 R. Tan, J. Zhou, Z. Yao, B. Wei and Z. Li, *Ceram. Int.*, 2021, **47**, 2077–2085.

5 F. Ghanbari, S. Moradi Dehaghi and H. Mahdavi, *J. Coat. Technol. Res.*, 2020, **17**, 815–826.

6 Y. Lian, B. Han, D. Liu, Y. Wang, H. Zhao, P. Xu, X. Han and Y. Du, *Nano-Micro Lett.*, 2020, **12**, 153.

7 P. Liu, S. Gao, W. Huang, J. Ren, D. Yu and W. He, *Carbon*, 2020, **159**, 83–93.

8 H. Lv, Z. Yang, P. L. Wang, G. Ji, J. Song, L. Zheng, H. Zeng and Z. J. Xu, *Adv. Mater.*, 2018, **30**, 1706343.

9 C. Wu, Z. Chen, M. Wang, X. Cao, Y. Zhang, P. Song, T. Zhang, X. Ye, Y. Yang, W. Gu, J. Zhou and Y. Huang, *Small*, 2020, **16**, 2001686.

10 M. Ning, P. Jiang, W. Ding, X. Zhu, G. Tan, Q. Man, J. Li and R. Li, *Adv. Funct. Mater.*, 2021, **31**, 2011229.

11 X. Zhang, J. Zhu, P. Yin, A. Guo, A. Huang, L. Guo and G. Wang, *Adv. Funct. Mater.*, 2018, **28**, 1800761.

12 F. Ye, Q. Song, Z. Zhang, W. Li, S. Zhang, X. Yin, Y. Zhou, H. Tao, Y. Liu, L. Cheng, L. Zhang and H. Li, *Adv. Funct. Mater.*, 2018, **28**, 1707205.

13 G. Logesh, U. Sabu, C. Srishilan, M. Rashad, A. Joseph, K. C. J. Raju and M. Balasubramanian, *Ceram. Int.*, 2021, **47**, 22540–22549.

14 Z. Wu, K. Pei, L. Xing, X. Yu, W. You and R. Che, *Adv. Funct. Mater.*, 2019, **29**, 1901448.

15 P. Liu, S. Gao, G. Zhang, Y. Huang, W. You and R. Che, *Adv. Funct. Mater.*, 2021, **31**, 2102812.

16 L. Wu, Y. Lu, W. Shao, H. Wei, G. Tong and W. Wu, *Adv. Mater. Interfaces*, 2020, **7**, 2000736.

17 H. Lv, Z. Yang, B. Liu, G. Wu, Z. Lou, B. Fei and R. Wu, *Nat. Commun.*, 2021, **12**, 834.

18 J. Shu, W. Cao and M. Cao, *Adv. Funct. Mater.*, 2021, **31**, 2100470.

19 X. Wang, W. Cao, M. Cao and J. Yuan, *Adv. Mater.*, 2020, **32**, 2002112.

20 R. Fan, B. Xiong, R. Peng and M. Wang, *Adv. Mater.*, 2020, **32**, 1904646.

21 Y. Guo, D. Wang, T. Bai, H. Liu, Y. Zheng, C. Liu and C. Shen, *Adv. Compos. Hybrid Mater.*, 2021, **4**, 602–613.

22 L. Wang, X. Yu, X. Li, J. Zhang, M. Wang and R. Che, *Chem. Eng. J.*, 2020, **383**, 123099.

23 Q. Wu, B. Wang, Y. Fu, Z. Zhang, P. Yan and T. Liu, *Chem. Eng. J.*, 2021, **410**, 128378.

24 G. Liu, X. Liu, Z. Song, X. Sun, Y. Li, J. Shui and R. Yu, *Chem. Eng. J.*, 2021, **417**, 128093.

25 X. Lu, D. Zhu, X. Li, M. Li, Q. Chen and Y. Qing, *Adv. Compos. Hybrid Mater.*, 2021, **4**, 946–956.

26 M. Zeng, Q. Cao, J. Liu, B. Guo, X. Hao, Q. Liu, X. Liu, X. Sun, X. Zhang and R. Yu, *ACS Appl. Mater. Interfaces*, 2020, **12**, 1222–1231.

27 J. Xiong, Z. Xiang, B. Deng, M. Wu, L. Yu, Z. Liu, E. Cui, F. Pan, R. Liu and W. Lu, *Appl. Surf. Sci.*, 2020, **513**, 145778.

This journal is © The Royal Society of Chemistry 2022

J. Mater. Chem. A, 2022, **10**, 1290–1298 | **1297**

28 R. Peymanfar and F. Fazlalizadeh, *Chem. Eng. J.*, 2020, **402**, 126089.

29 Q. Liu, X. Liu, H. Feng, H. Shui and R. Yu, *Chem. Eng. J.*, 2017, **314**, 320–327.

30 X. Xu, G. Wang, G. Wan, S. Shi, C. Hao, Y. Tang and G. Wang, *Chem. Eng. J.*, 2020, **382**, 122980.

31 X. Li, X. Yin, C. Song, M. Han, H. Xu, W. Duan, L. Cheng and L. Zhang, *Adv. Funct. Mater.*, 2018, **28**, 1803938.

32 X. Liang, Z. Man, B. Quan, J. Zheng, W. Gu, Z. Zhang and G. Ji, *Nano-Micro Lett.*, 2020, **12**, 102.

33 L. Wang, M. Huang, X. Yu, W. You, J. Zhang, X. Liu, M. Wang and R. Che, *Nano-Micro Lett.*, 2020, **12**, 150.

34 F. Pan, Z. Liu, B. Deng, Y. Dong, X. Zhu, C. Huang and W. Lu, *Nano-Micro Lett.*, 2021, **13**, 43.

35 Q. Song, F. Ye, X. Yin, W. Li, H. Li, Y. Liu, K. Li, K. Xie, X. Li, Q. Fu, L. Cheng, L. Zhang and B. Wei, *Adv. Mater.*, 2017, **29**, 1701583.

36 W.-L. Song, Y.-J. Zhang, K.-L. Zhang, K. Wang, L. Zhang, L.-L. Chen, Y. Huang, M. Chen, H. Lei, H. Chen and D. Fang, *Adv Sci*, 2020, **7**, 1902162.

37 X. Gao, X. Wu and J. Qiu, *Adv. Electron. Mater.*, 2018, **4**, 1700565.

38 N. L. Rosi, *Chem. Res. Chin. Univ.*, 2021, **37**, 187–188.

39 B. Wen, H. Yang, Y. Lin, L. Ma, Y. Qiu, F. Hu and Y. Zheng, *J. Mater. Chem. A*, 2021, **9**, 3567–3575.

40 J. Xu, R. Li, S. Ji, B. Zhao, T. Cui, X. Tan, G. Gou, J. Jian, H. Xu, Y. Qiao, Y. Yang, S. Zhang and T. Ren, *ACS Nano*, 2021, **15**, 8907–8918.

41 L. Hou, Y. Shi, S. Zhu, M. Rehan, G. Pang, X. Zhang and C. Yuan, *J. Mater. Chem. A*, 2017, **5**, 133–144.

42 W. H. Huang, X. M. Li, X. F. Yang, H. B. Zhang, F. Wang and J. Zhang, *Chem. Commun.*, 2021, **57**, 4847–4850.

43 J. Wang, L. Liu, S. Jiao, K. Ma, J. Lv and J. Yang, *Adv. Funct. Mater.*, 2020, **30**, 2002595.

44 F. Ran, X. Yang, X. Xu, S. Li, Y. Liu and L. Shao, *Chem. Eng. J.*, 2021, **412**, 128673.

45 Y. Zhu, X. Jiang, L. Lin, S. Wang and C. Chen, *Chem. Res. Chin. Univ.*, 2020, **36**, 1032–1038.

46 X. Wang, L. Zhuang, Y. Jia, L. Zhang, Q. Yang, W. Xu, D. Yang, X. Yan, L. Zhang, Z. Zhu, C. L. Brown, P. Yuan and X. Yao, *Chem. Res. Chin. Univ.*, 2020, **36**, 479–487.

47 Z. Zeng, T. Wu, D. Han, Q. Ren, G. Siqueira and G. Nyström, *ACS Nano*, 2020, **14**, 2927–2938.

48 F. Wang, Z. S. Liu, H. Yang, Y. X. Tan and J. Zhang, *Angew. Chem., Int. Ed.*, 2011, **50**, 450–453.

49 Y. Li, R. Zhang, W. Zhou, X. Wu, H. Zhang and J. Zhang, *ACS Nano*, 2019, **13**, 5533–5540.

50 D. Mao, J. Wan, J. Wang and D. Wang, *Adv. Mater.*, 2019, **31**, 1802874.

51 L. Wang, J. Wan, Y. Zhao, N. Yang and D. Wang, *J. Am. Chem. Soc.*, 2019, **141**, 2238–2241.

52 Y. T. Xu, Z. M. Ye, J. W. Ye, L. M. Cao, R. K. Huang, J. X. Wu, D. D. Zhou, X. F. Zhang, C. T. He, J. P. Zhang and X. M. Chen, *Angew. Chem., Int. Ed.*, 2019, **58**, 139–143.

53 W. Huang, Q. Li, D. Yu, Y. Tang, D. Lin, F. Wang and J. Zhang, *Inorg. Chem.*, 2021, **60**, 3074–3081.

1298 | *J. Mater. Chem. A*, 2022, **10**, 1290–1298

This journal is © The Royal Society of Chemistry 2022